

A two-qubit logic gate in silicon

M. Veldhorst¹, C. H. Yang¹, J. C. C. Hwang¹, W. Huang¹, J. P. Dehollain¹, J. T. Muhonen¹, S. Simmons¹, A. Laucht¹, F. E. Hudson¹, K. M. Itoh², A. Morello¹ & A. S. Dzurak¹

Quantum computation requires qubits that can be coupled in a scalable manner, together with universal and high-fidelity one- and two-qubit logic gates^{1,2}. Many physical realizations of qubits exist, including single photons³, trapped ions⁴, superconducting circuits⁵, single defects or atoms in diamond^{6,7} and silicon⁸, and semiconductor quantum dots⁹, with single-qubit fidelities that exceed the stringent thresholds required for fault-tolerant quantum computing¹⁰. Despite this, high-fidelity two-qubit gates in the solid state that can be manufactured using standard lithographic techniques have so far been limited to superconducting qubits⁵, owing to the difficulties of coupling qubits and dephasing in semiconductor systems^{11–13}. Here we present a two-qubit logic gate, which uses single spins in isotopically enriched silicon¹⁴ and is realized by performing single- and two-qubit operations in a quantum dot system using the exchange interaction, as envisaged in the Loss–DiVincenzo proposal². We realize CNOT gates via controlled-phase operations combined with single-qubit operations. Direct gate-voltage control provides single-qubit addressability, together with a switchable exchange interaction that is used in the two-qubit controlled-phase gate. By independently reading out both qubits, we measure clear anticorrelations in the two-spin probabilities of the CNOT gate.

Quantum dots have long been considered an attractive physical platform for quantum information processing². Large arrays can be conveniently realized using conventional lithographic approaches. Initialization, read-out, control and coupling can be achieved through local electrical pulses, possibly in combination with magnetic resonance techniques. Early research focused mainly on III–V semiconductor compounds such as GaAs, resulting in single-spin qubits¹⁵, singlet-triplet qubits¹⁶ and exchange-only qubits¹⁷, which can be coupled capacitively¹¹ or via the exchange interaction^{12,13}. Although these approaches demonstrate the potential of quantum-dot qubits, strong dephasing due to the nuclear spin background has limited the quality of the quantum operations. A marked improvement in coherence times has been observed by defining the quantum dots in silicon^{9,18,19}, which can be isotopically purified¹⁴, such that quantum dots with single-spin fidelities above the threshold of surface codes¹⁰ can be realized⁹.

A scalable approach towards quantum computation ideally requires that the coupling between qubits can be turned on and off², so that single- and two-qubit operations can be selectively chosen. Here, we push silicon-based quantum information processing beyond the single-qubit level by realizing a controlled-phase (CZ) gate, which is commonly used in superconducting qubits⁵ and has been theoretically discussed for quantum-dot systems²⁰. This two-qubit gate, together with single-qubit gates, provides all of the necessary operations for universal quantum computation. In our system, each qubit is defined by the spin state of a single electron, with energies split by a large magnetic field of strength $B_0 = 1.4$ T. The single-qubit states are manipulated using spin-resonance techniques, through the local application of an oscillating magnetic field produced by an on-chip electron spin resonance (ESR) line. By exploiting the Stark shift, we electrically control the effective

g -factor of the qubits, to tune the Zeeman energy $E_Z = g\mu_B B_0$ and the associated qubit resonance frequency $\nu = E_Z/h$ for selective qubit control⁹, where μ_B is the Bohr magneton and h is the Planck constant. The two-qubit gate is then realized using electrical pulses that control the exchange coupling between the qubits.

Figure 1a shows a schematic and Fig. 1b shows a scanning electron microscope image of the double-quantum-dot structure fabricated on a ²⁸Si epilayer with a residual ²⁹Si concentration of 800 p.p.m. (ref. 14). The device consists of three aluminium layers, nine aluminium gates, an aluminium lead for ESR control²¹, and source, drain and reservoir leads that connect to a gate-induced two-dimensional electron gas using multilevel gate-stack silicon metal–oxide–semiconductor technology²². A single-electron transistor (SET) is formed to monitor the charge state of the quantum-dot system and for spin read-out using spin-to-charge conversion²³. For both our single- and two-qubit experiments, we tune the gate voltages to the appropriate dc operating regime and then adjust gate G_1 for qubit read-out, initialization and control.

Figure 1c shows the stability diagram of the double-quantum-dot system with charge occupancy (N_2, N_1) . The charge transitions of quantum dots D_1 and D_2 , which are underneath gates G_1 and G_2 , respectively, are distinguished by their gate voltage dependence and their capacitive coupling to the SET. We define qubit Q_1 by loading a single electron into D_1 , so that $N_1 = 1$; similarly for qubit Q_2 , we have $N_2 = 1$.

To characterize the individual qubits, we bias the gate voltages such that the tunnel time of the respective qubit to the reservoir is approximately 100 μ s and both qubits are measured in the $(1, 1)$ charge state. Clear Rabi oscillations are observed as a function of microwave pulse time τ_p for both qubits, as shown in Fig. 1d. Q_1 has a dephasing time of $T_2^* = 120$ μ s, with a coherence time T_2 that can be extended up to 28 ms using CPMG (Carr–Purcell–Meiboom–Gill) pulses⁹, and Q_2 has a dephasing time of $T_2^* = 61$ μ s (see Supplementary Information section 3).

We couple the qubits via the exchange interaction, as discussed in ref. 2, with an exchange coupling that is electrically controlled via the detuning energy ϵ (see Fig. 2a, b). We control the system in the $(1, 1)$ region, and read out Q_2 at the $(1, 1)$ – $(0, 1)$ transition and Q_1 at the $(0, 1)$ – $(0, 0)$ transition.

The presence of a sharp interface and large perpendicular electric fields increases the energy of all excited states²⁴, and allows us to consider only the lowest five energy states¹⁶ (see also Supplementary Information section 2). We can consequently describe the system in the rotating-wave approximation in the basis $[|Q_2, Q_1\rangle, \Psi = \{|\uparrow, \uparrow\rangle, |\uparrow, \downarrow\rangle, |\downarrow, \uparrow\rangle, |\downarrow, \downarrow\rangle, |0, 2\rangle\}]$, with the effective Hamiltonian

$$H = \begin{bmatrix} \overline{E_Z} - \nu & \Omega & \Omega & 0 & 0 \\ \Omega & \delta E_Z/2 & 0 & \Omega & t_0 \\ \Omega & 0 & -\delta E_Z/2 & \Omega & -t_0 \\ 0 & \Omega & \Omega & -\overline{E_Z} + \nu & 0 \\ 0 & t_0 & -t_0 & 0 & U - \epsilon \end{bmatrix} \quad (1)$$

¹Centre for Quantum Computation and Communication Technology, School of Electrical Engineering and Telecommunications, The University of New South Wales, Sydney, New South Wales 2052, Australia. ²School of Fundamental Science and Technology, Keio University, 3-14-1 Hiyoshi, Kohoku-ku, Yokohama 223-8522, Japan.

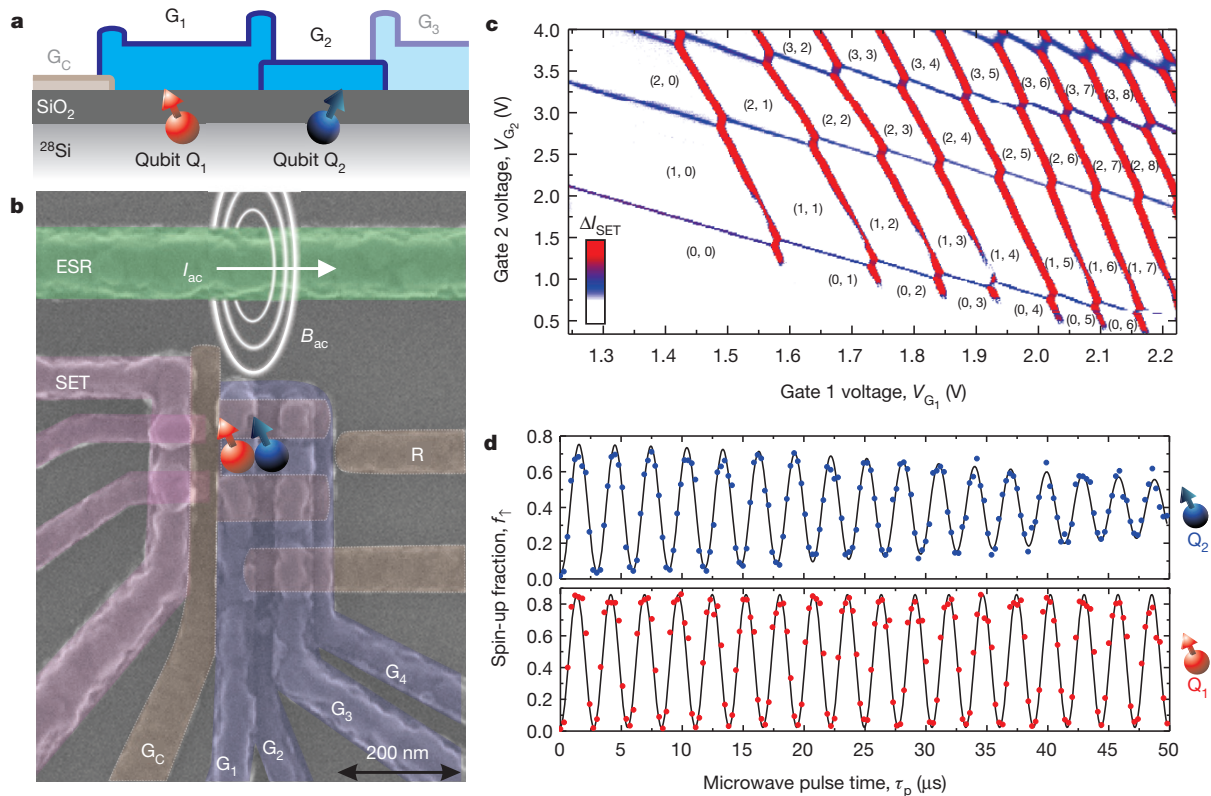


Figure 1 | Silicon two-qubit logic device, incorporating SET read-out and selective qubit control. **a**, **b**, Schematic (**a**) and scanning electron microscope coloured image (**b**) of the device. The quantum dot structure (labels G_C and G_{1-4}) can be operated as a single or double quantum dot by appropriate biasing of gate electrodes G_1 – G_4 , where we choose here to confine the dots $D_{1,2}$ underneath gates $G_{1,2}$, respectively. The confinement gate G_C runs underneath G_1 – G_3 and confines the quantum dot on all sides except on the reservoir (R) side. Qubit operation is achieved via an ac current I_{ac} through the ESR line, resulting in an ac magnetic field B_{ac} . **c**, Stability diagram of the double quantum dot obtained by monitoring the current I_{SET} through the capacitively coupled SET. The numbers in parentheses are the change occupancies of $D_{2,1}$: (N_2, N_1) .

The difference in distance to the SET results in different capacitive coupling, such that the individual dots can be easily distinguished. The tunnel coupling of the fourth transition ($N_1 = 3 \rightarrow 4$) of D_1 is relatively weak, which is due to valley and spin filling, because there is only one state in the lowest orbital that can be occupied. Q_1 and Q_2 are realized by depleting D_1 and D_2 to the last electron. **d**, The quantum dot qubits can be individually controlled by electrically tuning the ESR resonance frequency using the Stark shift⁹. Clear Rabi oscillations for both qubits are observed. All measurements were performed in a dilution refrigerator with base temperature $T \approx 50$ mK and a dc magnetic field of strength $B_0 = 1.4$ T.

where $\overline{E_Z}$ is the mean Zeeman energy, δE_Z is the difference in Zeeman energy between the dots, Ω is the Rabi frequency, ν is the microwave frequency and t_0 is the tunnel coupling; for simplicity we have scaled the system such that $\hbar = 1$. In the experiments, we control ϵ by fast pulsing only on G_1 . The read-out on Q_2 (R_2) and control (C) bias points are depicted in Fig. 2a; we pulse close to the $(1, 1) \rightarrow (1, 2)$ transition, which has the same energy level structure as the $(1, 1) \rightarrow (0, 2)$ transition, shown in Fig. 2b. Single-qubit operations are realized with Rabi frequency Ω , by matching ν to the resonance frequency of one of the qubits. The presence of exchange coupling between the qubits alters the Zeeman levels as shown in Fig. 2b, where the finite coupling between the qubits causes an anticrossing between the $|0, 2\rangle$ and $|1, 1\rangle$ states. We experimentally map out the energy levels in the vicinity of the anticrossing, as shown in Fig. 2c, d.

In Fig. 2c, we have initialized Q_1 and Q_2 to spin down and, by applying a π -pulse to Q_2 (π_{X,Q_2}), we map out the resonance frequency of Q_2 as a function of detuning. We measure exchange couplings of more than 10 MHz, above which T_2^* of Q_2 becomes shorter than the π -pulse time $\tau_\pi = 1.5$ μ s and so spin flips cannot occur.

Initialization of antiparallel spin states is possible by pulsing to the $(1, 2)$ and returning to the $(1, 1)$ charge states (labelled I_{AP} in Fig. 2a). In this sequence, an electron tunnels from D_2 to D_1 (I in Fig. 2d) followed by an electron tunnelling from the reservoir R to D_2 (II in Fig. 2d). After returning to $(1, 1)$, the electron from D_2 tunnels back to R (III in Fig. 2d), and one of the two electrons on D_1 , which are in a

singlet state, tunnels to D_2 (IV in Fig. 2d). With this initialization into an antiparallel spin state, when we apply a microwave pulse on Q_2 , the spin-up fraction f_1 approaches 1/2, except when the microwave frequency matches a resonance frequency of Q_2 . Owing to the finite exchange interaction, there are two resonance frequencies. The lower frequency rotates the antiparallel state towards a combination of $|\downarrow, \downarrow\rangle$ and $|\downarrow, \uparrow\rangle$, where Q_2 always ends up as spin down. The higher frequency rotates the antiparallel state towards a combination of $|\uparrow, \downarrow\rangle$ and $|\uparrow, \uparrow\rangle$, where Q_2 always ends up as spin up. The results are depicted in Fig. 2d, which shows a decrease in f_1 at the lower branch and an increase of f_1 at the upper branch, demonstrating an exchange spin funnel, where both branches are visible (see Supplementary Information section 4 for further details). The two-qubit gate is conveniently realized using a quantum dot CZ gate²⁰ (see Supplementary Information section 6 for theoretical details). This approach allows individual control over the qubits in the absence of interaction and its associated noise, while using the coupling to perform two-qubit operations with a frequency that can be much higher than the single-qubit Rabi rotation frequency.

As described by equation (1) and depicted in Fig. 2b, changing ϵ modifies the qubit resonance frequencies of Q_1 and Q_2 and introduces an effective detuning frequency $\nu_{\uparrow\downarrow,(\uparrow\downarrow)}$, such that one qubit acquires a time-integrated phase shift $\phi_{\uparrow\downarrow,(\uparrow\downarrow)}$ that depends on the \hat{z} component of the spin state of the other qubit, and vice versa. The exchange coupling and $\nu_{\uparrow\downarrow,(\uparrow\downarrow)}$ are maximized at the anticrossing $\epsilon = U$; see Fig. 2b. When

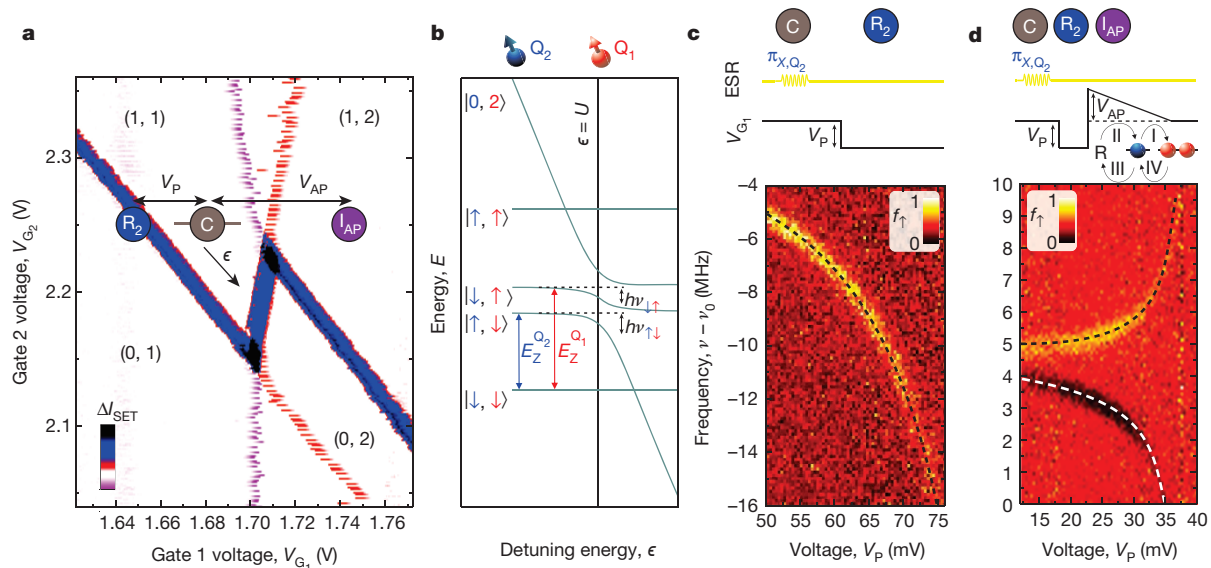


Figure 2 | Exchange spin funnel. **a**, Close up of the operation regime of the $(1, 1) \rightarrow (0, 2)$ charge states. We lowered the R–D₂ coupling so that the tunnelling time is approximately 100 μ s, matching the qubit experiments. In this range of weak R–D₁ coupling, the emptying and filling of D₁ is hysteretic with gate voltage, because the mutual charging energy becomes relevant²⁷, as D₁ can only tunnel when it aligns in energy with D₂. R₂ represents the read-out on Q₂; I_{AP} represents the antiparallel initialization. **b**, Schematic of the coupling between Q₁ and Q₂ using the exchange interaction at the $|1, 1\rangle \rightarrow |0, 2\rangle$ transition. By electrically tuning the g factors⁹ of Q₁ and Q₂, we control the individual qubit resonance frequencies over 10 MHz. Here, we tune to a frequency difference of

40 MHz (the difference is exaggerated in the schematic for clarity) for individual qubit control. **c**, ESR spectrum of the $|\downarrow, \downarrow\rangle \rightarrow |\uparrow, \downarrow\rangle$ transition as a function of increasing detuning. The data have been offset by a frequency $\nu_0 = 39.14$ GHz and the spin-up fractions are normalized for clarity. The dashed lines are fits using equation (1) and assuming $t_0 = 900$ MHz, a Stark shift of 19 MHz V^{-1} , and that the top gates have a lever arm of 0.2 eV V^{-1} . **d**, As for **c**, but with an additional pulse of amplitude V_{AP} (see schematic) so that we initialize antiparallel spin states (AP) and observe both the $|\uparrow, \downarrow\rangle \rightarrow |\downarrow, \downarrow\rangle$ and $|\downarrow, \downarrow\rangle \rightarrow |\uparrow, \downarrow\rangle$ transitions. The labels I–IV indicate electron tunnelling between R and D_{1,2}; see text for details.

a CZ operation is performed such that $\phi_{\uparrow\downarrow} + \phi_{\downarrow\uparrow} = \pi$, the operation differs only by an overall phase from the basis CZ gate²⁵. This overall phase can be removed using single-qubit pulses or via voltage pulses exploiting the Stark shift⁹. To realize a CNOT operation using the CZ gate, a CZ(π) rotation is performed in between two $\pi/2$ -pulses on Q₂ that have a phase difference $\phi_{\uparrow\downarrow}$.

Figure 3a shows the spin-up fraction f_{\uparrow} of Q₂ after applying a $(\pi/2)_X$ -pulse and a $(\pi/2)_Y$ -pulse on Q₂ separated by an interaction time τ_Z with increasing exchange coupling, set via ϵ and tuned by the voltage V_{CZ} . Plotting the frequency $\nu_{\uparrow\downarrow}$ as a function of V_{CZ} (Fig. 3b) gives a trend consistent with that observed via ESR mapping, as shown in Fig. 2c, d. The two-qubit dephasing time $T_{2,CZ}^*$ is the free induction decay time of

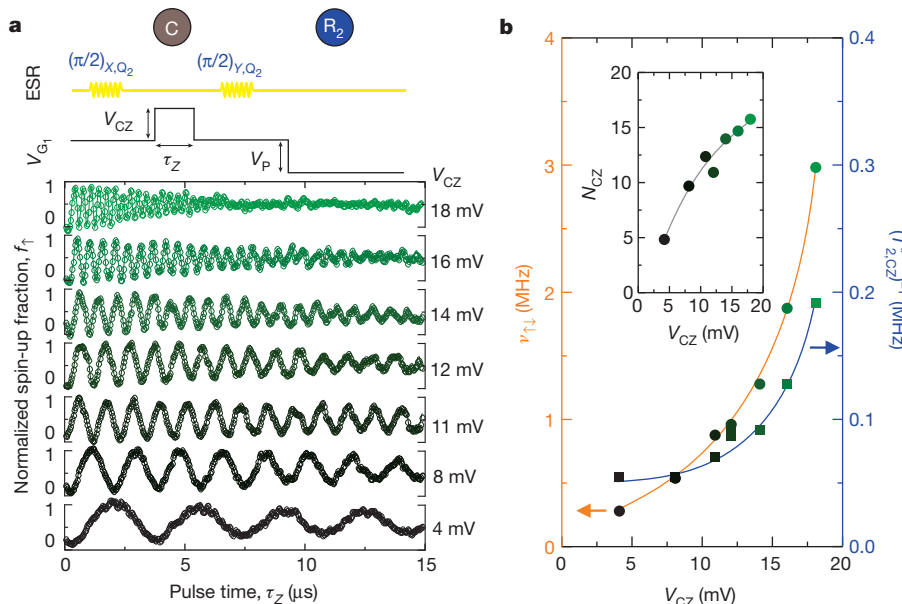


Figure 3 | Controlled phase (CZ) gate operation time. **a**, Spin-up fraction after applying a $(\pi/2)_X$ -pulse, a CZ operation and a $(\pi/2)_Y$ -pulse, for increasing qubit interaction. The exchange coupling is controlled via ϵ , set with V_{G1} , resulting in a tunable two-qubit operation frequency $\nu_{\uparrow\downarrow}$. **b**, By fitting the data in **a**, we map out $\nu_{\uparrow\downarrow}$ and $T_{2,CZ}^*$ as a function of V_{CZ} . The orange and blue colouring

and the arrows indicate the axis each data set corresponds to; the colouring of the data corresponds to that in **c**, indicating V_{CZ} . The inset shows the number of possible CZ rotations N_{CZ} . Although $T_{2,CZ}^*$ decreases with coupling, the number of possible two-qubit rotations continues to increase.

the two-qubit system. At large values of detuning ($\epsilon \rightarrow \infty$) or when the interaction vanishes ($t_0 \rightarrow 0$), $T_{2,CZ}^*$ reduces to the single-qubit Ramsey T_2^* . We obtain $T_{2,CZ}^*$ by fitting an exponential to the decay of the oscillations in Fig. 3a. These values of $T_{2,CZ}^*$ are plotted along with the measured $v_{\uparrow\downarrow}$ values in Fig. 3b. We find that the two-qubit dephasing rate $(T_{2,CZ}^*)^{-1}$ rises in step with the exchange coupling and $v_{\uparrow\downarrow}$, which is to be expected because $\delta v_{\uparrow\downarrow}/\delta V$ also increases with $v_{\uparrow\downarrow}$, meaning that the qubit system becomes increasingly sensitive to electrical noise²⁶. Despite this, the total number of oscillations $N_{CZ} = v_{\uparrow\downarrow} T_{2,CZ}^*$ also increases with $v_{\uparrow\downarrow}$, as shown in Fig. 3b. In Supplementary Information section 7, we show an optimized sequence where $T_{2,CZ}^* = 8.3 \mu\text{s}$ and $v_{\uparrow\downarrow} = 3.14 \text{ MHz}$, such that $N_{CZ} > 26$.

For all of the experiments described in Figs 2 and 3, we performed read-out only on Q_2 , owing to its proximity to the reservoir used for spin selective read-out. However, to demonstrate a two-qubit CNOT gate it is desirable to read out the state of both qubits, allowing the observation of non-classical correlations. This requires a more complex pulsing protocol on G_1 (Fig. 4a), to first read Q_2 at the charge transition $(0,0)-(0,1)$, subsequently read and initialize Q_1 at

the $(0,1)-(1,1)$ transition, and initialize Q_2 at the $(0,0)-(0,1)$ transition. The read-out ($R_{1,2}$) and control (C) bias points are shown on the charge stability map in Fig. 4b. Following two-qubit read-out of the previous state, the system is prepared as $|\downarrow, \downarrow\rangle$, after which single-qubit rotations are applied to each qubit to prepare any desired initial two-qubit state.

Figure 4c shows the measured states of Q_1 and Q_2 after applying the CZ gate as a function of τ_Z , with Q_1 initialized to $|\uparrow\rangle$ (top panel) and $|\downarrow\rangle$ (bottom panel). As expected, the control qubit Q_1 (red) is not perturbed when exchange is turned on because it is in a basis state; however, the target qubit Q_2 (blue) is initialized to $\frac{1}{\sqrt{2}}(|\uparrow\rangle + |\downarrow\rangle)$ with a $(\pi/2)_X$ -pulse on Q_2 and so rotates about the equator of the Bloch sphere when exchange is turned on for time τ_Z . The strength of the exchange coupling is set so that Q_2 rotates about the Bloch sphere at double the frequency for $Q_1 = |\downarrow\rangle$ than for $Q_1 = |\uparrow\rangle$; this is reflected in the final state of Q_2 plotted in Fig. 4c (see Supplementary Information section 8 for further details). A CZ gate is realized at $\tau_Z = 480 \text{ ns}$, when $\phi_{\uparrow\downarrow} + \phi_{\downarrow\uparrow} = \pi$, and this is converted to a CNOT gate (the target qubit is

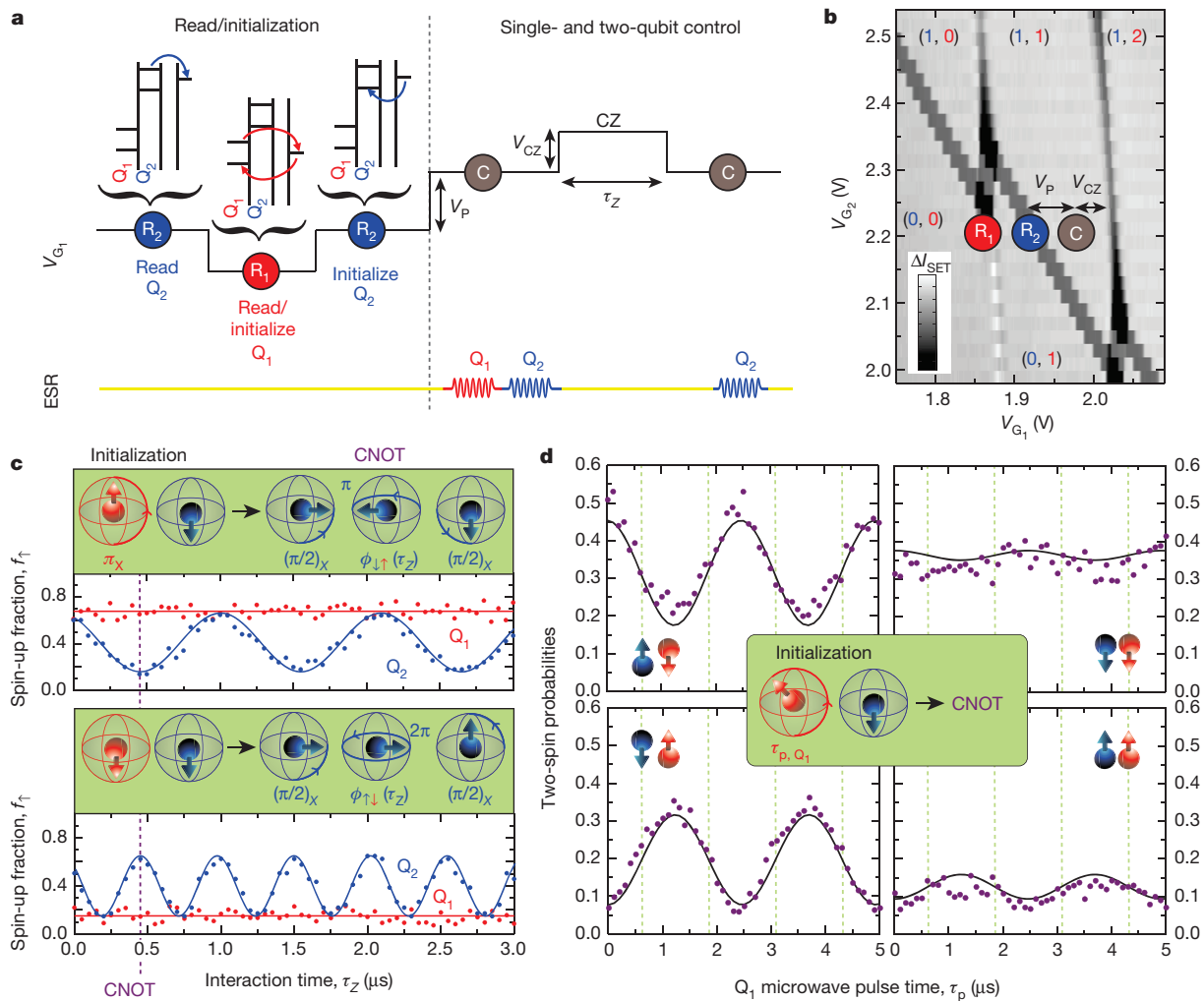


Figure 4 | Two-spin correlations for a two-qubit logic gate. **a**, Pulsing protocol for two-qubit read-out and single- and two-qubit operations. After read-out of Q_2 (R_2) and Q_1 (R_1), we pulse back to (R_2) to ensure proper initialization. Individual qubit operations are performed with high ϵ , whereas the CZ operation occurs in the presence of interaction. **b**, Stability diagram showing the operation regime. **c**, Spin-up fraction of both qubits after initializing Q_1 spin up (top) and spin down (bottom) using a microwave pulse and applying a controlled rotation using Q_2 as the target qubit. A CNOT gate is achieved in 480 ns, as indicated by the dotted purple line (see inset for the

corresponding Bloch sphere animation). **d**, Two-spin probabilities as functions of the microwave pulse length on Q_1 after applying a CNOT gate (see inset for the corresponding Bloch sphere animation), showing clear anticorrelations between the two qubit spin states. The different plots correspond to different spin states of $Q_{1,2}$, as indicated. The black lines correspond to fits based on a CNOT gate, and include the experimental read-out errors (see Supplementary Information section 9). The green dotted lines correspond to the intended maximally entangled states.

flipped when the control qubit is $|\downarrow\rangle$ by applying $(\pi/2)_X$ -pulses on Q_2 before and after the CZ.

We use the CNOT gate to create an entangled state of Q_1 and Q_2 . To realize this, we initialize the qubits first to the $|\downarrow, \downarrow\rangle$ state, then apply a varying microwave pulse time to rotate Q_1 into superposition states, with a Rabi time $\tau_{\text{Rabi}} = 2.4 \mu\text{s}$, and finally apply the CNOT gate. To demonstrate the CNOT gate, we convert the individual qubit spin-up fractions into two-spin probabilities; Fig. 4d shows the four possible two-spin probabilities. Clear oscillations are observed in the probabilities of the antiparallel states, $P(|\downarrow, \uparrow\rangle)$ and $P(|\uparrow, \downarrow\rangle)$, whereas these oscillations are almost absent in the probabilities of the parallel states, $P(|\downarrow, \downarrow\rangle)$ and $P(|\uparrow, \uparrow\rangle)$, thereby demonstrating the anticorrelations expected for the CNOT gate. The hints of oscillations in the symmetric spin states are probably due to read errors (which are included in the fitted line in Fig. 4d, see also Supplementary Information section 9); our current visibilities are not sufficient to demonstrate violation of the Bell inequality.

Future experiments will include improvements to the read-out fidelities, thus facilitating full two-qubit tomography. The qubit control fidelities could be further improved by lowering the sensitivity to electrical noise. Although these silicon qubits represent the smallest scalable two-qubit system reported so far, the complete fabrication process is compatible with standard CMOS (complementary metal-oxide-semiconductor) technology, and is also consistent with current transistor feature sizes, offering the prospect of realizing a large-scale quantum processor using the same silicon manufacturing technologies that have enabled the current information age.

Received 7 November 2014; accepted 22 July 2015.

Published online 5 October 2015.

- DiVincenzo, D. P. The physical implementation of quantum computation. *Fortschr. Phys.* **48**, 771–783 (2000).
- Loss, D. & DiVincenzo, D. P. Quantum computation with quantum dots. *Phys. Rev. A* **57**, 120–126 (1998).
- Kok, P. *et al.* Linear optical quantum computing with photonic qubits. *Rev. Mod. Phys.* **79**, 135–174 (2007).
- Brown, K. R. *et al.* Single-qubit-gate error below 10^{-4} in a trapped ion. *Phys. Rev. A* **84**, 030303 (2011).
- Barends, R. *et al.* Superconducting quantum circuits at the surface code threshold for fault tolerance. *Nature* **508**, 500–503 (2014).
- Waldherr, G. *et al.* Quantum error correction in a solid-state hybrid spin register. *Nature* **506**, 204–207 (2014).
- Dolde, F. *et al.* High-fidelity spin entanglement using optimal control. *Nature Commun.* **5**, 3371 (2014).
- Muhonen, J. T. *et al.* Storing quantum information for 30 seconds in a nanoelectronic device. *Nature Nanotechnol.* **9**, 986–991 (2014).
- Veldhorst, M. *et al.* An addressable quantum dot qubit with fault-tolerant fidelity. *Nature Nanotechnol.* **9**, 981–985 (2014).
- Fowler, A., Mariantoni, M., Martinis, J. M. & Cleland, A. N. Surface codes: towards practical large-scale quantum computation. *Phys. Rev. A* **86**, 032324 (2012).
- Shulman, M. D. *et al.* Demonstration of entanglement of electrostatically coupled singlet-triplet qubits. *Science* **336**, 202–205 (2012).
- Nowack, K. C. *et al.* Single-shot correlations and two-qubit gate of solid-state spins. *Science* **333**, 1269–1272 (2011).
- Brunner, R. *et al.* Two-qubit gate of combined single-spin rotation and interdot exchange in a double quantum dot. *Phys. Rev. Lett.* **107**, 146801 (2011).
- Itoh, K. M. & Watanabe, H. Isotope engineering of silicon and diamond for quantum computing and sensing applications. *Mater. Res. Soc. Commun.* **4**, 143–157 (2014).
- Koppens, F. H. L. *et al.* Driven coherent oscillations of a single electron spin in a quantum dot. *Nature* **442**, 766–771 (2006).
- Petta, J. R. *et al.* Coherent manipulation of coupled electron spins in semiconductor quantum dots. *Science* **309**, 2180–2184 (2005).
- Medford, J. *et al.* Self-consistent measurement and state tomography of an exchange-only spin qubit. *Nature Nanotechnol.* **8**, 654–659 (2013).
- Maune, B. M. *et al.* Coherent singlet-triplet oscillations in a silicon-based double quantum dot. *Nature* **481**, 344–347 (2012).
- Kawakami, E. *et al.* Electrical control of a long-lived spin qubit in a Si/SiGe quantum dot. *Nature Nanotechnol.* **9**, 666–670 (2014).
- Meunier, T., Calado, V. E. & Vandersypen, L. M. K. Efficient controlled-phase gate for single-spin qubits in quantum dots. *Phys. Rev. B* **83**, 121403(R) (2011).
- Dehollain, J. P. *et al.* Nanoscale broadband transmission lines for spin qubit control. *Nanotechnology* **24**, 015202 (2013).
- Angus, S. J., Ferguson, A. J., Dzurak, A. S. & Clark, R. G. Gate-defined quantum dots in intrinsic silicon. *Nano Lett.* **7**, 2051–2055 (2007).
- Elzerman, J. M. *et al.* Single-shot read-out of an individual electron spin in a quantum dot. *Nature* **430**, 431–435 (2004).
- Yang, C. H. *et al.* Spin-valley lifetimes in a silicon quantum dot with tunable valley splitting. *Nature Commun.* **4**, 2069 (2013).
- Ghosh, J. *et al.* High-fidelity controlled- σ^z gate for resonator-based superconducting quantum computers. *Phys. Rev. A* **87**, 022309 (2013).
- Dial, O. E. *et al.* Charge noise spectroscopy using coherent exchange oscillations in a singlet-triplet qubit. *Phys. Rev. Lett.* **110**, 146804 (2013).
- Yang, C. H. *et al.* Charge state hysteresis in semiconductor quantum dots. *Appl. Phys. Lett.* **105**, 183505 (2014).

Supplementary Information is available in the online version of the paper.

Acknowledgements We thank S. Bartlett for discussions and C. M. Cheng for contributions to the preparation of the experimental setup. We acknowledge support from the Australian Research Council (CE11E0001017), the US Army Research Office (W911NF-13-1-0024) and the NSW Node of the Australian National Fabrication Facility. M.V. acknowledges support from the Netherlands Organization for Scientific Research (NWO) through a Rubicon Grant. The work at Keio was supported in part by the Grant-in-Aid for Scientific Research by MEXT, in part by NanoQuine, in part by FIRST and in part by the JSPS Core-to-Core Program.

Author Contributions M.V., C.H.Y. and J.C.C.H. performed the experiments. M.V. and F.E.H. fabricated the devices. K.M.I. prepared and supplied the ^{28}Si epilayer wafer. W.H., J.P.D., J.T.M., S.S. and A.L. contributed to the preparation of the experiments. M.V., C.H.Y., A.M. and A.S.D. designed the experiment and discussed the results. M.V. analysed the results. M.V. and A.S.D. wrote the manuscript with input from all co-authors.

Author Information Reprints and permissions information is available at www.nature.com/reprints. The authors declare no competing financial interests. Readers are welcome to comment on the online version of the paper. Correspondence and requests for materials should be addressed to M.V. (M.Veldhorst@unsw.edu.au) or A.S.D. (A.Dzurak@unsw.edu.au).